

LA-UR-16-23474

Approved for public release; distribution is unlimited.

Title: Milestone report: The simulation of radiation driven gas diffusion in UO₂ at low temperature

Author(s): Cooper, Michael William Donald
Kuganathan, Navaratnarajah
Burr, Patrick A
Rushton, Michael J. D.
Grimes, Robin W
Turbull, James Anthony
Stanek, Christopher Richard
Andersson, Anders David Ragnar

Intended for: Report

Issued: 2016-10-24 (rev.1)

Disclaimer:

Los Alamos National Laboratory, an affirmative action/equal opportunity employer, is operated by the Los Alamos National Security, LLC for the National Nuclear Security Administration of the U.S. Department of Energy under contract DE-AC52-06NA25396. By approving this article, the publisher recognizes that the U.S. Government retains nonexclusive, royalty-free license to publish or reproduce the published form of this contribution, or to allow others to do so, for U.S. Government purposes. Los Alamos National Laboratory requests that the publisher identify this article as work performed under the auspices of the U.S. Department of Energy. Los Alamos National Laboratory strongly supports academic freedom and a researcher's right to publish; as an institution, however, the Laboratory does not endorse the viewpoint of a publication or guarantee its technical correctness.

Milestone report: The simulation of radiation driven gas diffusion in UO_2 at low temperature

M. W. D. Cooper^a, N. Kuganathan^b, P. A. Burr^c, M. J. D. Rushton^b, R. W. Grimes^b, J. A. Turnbull^d, C. R. Stanek^a, D. A. Andersson^a

^aMaterials Science and Technology Division, Los Alamos National Laboratory P.O. Box 1663, Los Alamos, NM 87545, USA

^bDepartment of Materials, Imperial College London, London, SW7 2AZ, UK

^cSchool of Electrical Engineering and Telecommunications, University of New South Wales, Kensington, 2052, NSW, Australia.

^dIndependent Consultant, UK

Abstract

Below 1000 K it is thought that fission gas diffusion in nuclear fuel during irradiation occurs through atomic mixing due to radiation damage. This is an important process for nuclear reactor performance as it affects fission gas release, particularly from the periphery of the pellet where such temperatures are normal. Here we present a molecular dynamics study of Xe and Kr diffusion due to irradiation. Thermal spikes and cascades have been used to study the electronic stopping and ballistic phases of damage respectively. Our results predict that O and Kr exhibit the greatest diffusivity and U the least, while Xe lies in between. It is concluded that the ballistic phase does not sufficiently account for the experimentally observed diffusion. Preliminary thermal spike calculations indicate that the electronic stopping phase generates greater fission gas displacement than the ballistic phase, although further calculation must be carried out to confirm this.

A good description of the system by the empirical potentials is important over the very wide temperatures induced during thermal spike and damage cascade simulations. This has motivated the development of a parameter set for gas-actinide and gas-oxygen interactions that is complementary for use with a recent many-body potential set. A comprehensive set of density functional theory (DFT) calculations were used to study Xe and Kr incorporation at a number of sites in CeO_2 , ThO_2 , UO_2 and PuO_2 . These structures were used to fit a potential, which was used to generate molecular dynamics (MD) configurations incorporating Xe and Kr at 300 K, 1500 K, 3000 K and 5000 K. Subsequent matching to the forces predicted by DFT for these MD configurations was used to refine the potential set. This fitting approach ensured weighted fitting to configurations that are thermodynamically significant over a broad temperature range, while avoiding computationally expensive DFT-MD calculations. The resultant gas potentials were validated against DFT binding energies and are suitable for simulating combinations of Xe and Kr in solid solutions of CeO_2 , ThO_2 , UO_2 and PuO_2 , providing a powerful tool for the atomistic simulation of conventional nuclear reactor fuel UO_2 as well as advanced MOX fuels.

1. Introduction

The pre-eminent nuclear fuel has been UO_2 for several decades due to its radiation tolerance, high melting point and ability to accommodate the significant chemical changes experi-

Email address: cooper_m@lanl.gov, mwdc09@gmail.com (M. W. D. Cooper)

enced during reactor operation [1]. A particular problem for nuclear fuel is the release of the fission gases Xe and Kr from the pellet and into the helium-filled clad-pellet gap. This has the combined effect of reducing thermal conductivity and increasing the pressure of the plenum or cladding [2]. Other than causing an increased risk of centerline pellet melting, the high temperatures arising due to poor gap thermal conductivity also give rise to higher mobility and additional release of fission gases [3–5], further exacerbating the problem. A mitigating factor could be an increase in pellet thermal conductivity as the concentration of fission gas in solution in UO_2 is reduced [6]. Nonetheless, an eventual consequence of continued fission gas release is the rupturing of the cladding material and this represents a very real problem for nuclear reactor operation. As discussed by Turnbull *et al.* [7] there are three regimes for gas diffusion: i) higher temperature (> 1500 K) intrinsic diffusion, ii) intermediate temperature radiation enhanced diffusion and iii) the low temperature (< 1000 K) irradiation induced athermal contribution. In the latter case, which is commensurate with temperatures in the periphery of the fuel pellet, it is thought that the atomic mixing, which occurs during damage, drives gas mobility. An additional complexity arises during burn-up as U is transmuted to other actinides, in particular Pu^{239} . Alternatively, PuO_2 [8, 9] or ThO_2 [10] can be blended with UO_2 to form MOX fuels. It is, therefore, important to consider how such changes to the host lattice could alter fission gas behaviour and impact fuel performance. The use of Ce as a surrogate for Pu [11] or U [12] means CeO_2 is also of interest.

The underlying mechanisms for fission gas behaviour, as discussed, are complex and inter-related, whereby the temperature and radiation flux in the pellet have important effects [7]. There has been a strong focus on investigating the impact of fission gas on thermal conductivity [6], fission gas mobility in the bulk lattice or at extended defects [3–5, 13, 14] and the behaviour of fission gas bubbles [15–17]. By understanding and predicting these processes over a range of conditions, in particular a large temperature range, a greater understanding of fuel behaviour can be achieved. However, the accuracy of atomic scale simulations is underpinned by the models and theories upon which they are based. In particular, MD simulations are highly dependent upon the ability of a parameter set to accurately describe the properties of both the host UO_2 (or MOX) and the interaction of fission gas with the host lattice. Previously, Cooper, Rushton and Grimes (CRG) developed a many-body potential for pure actinide oxides and their mixed oxides [18–20]. The potential is capable of accurately predicting a large number of the thermophysical properties of these systems from 300 K to 3000 K. In particular, this is the first instance of an empirical potential being able to reproduce the bulk modulus of UO_2 from 300 K to 3000 K. Here we build upon this work by developing potentials for gas-oxygen and gas-actinide interactions that are consistent with this many-body actinide oxide potential set and that will enable the behaviour of fission gases in mixed oxides to be investigated. A combined classical MD and DFT force matching fitting approach will be presented. The new model is validated against literature and newly presented DFT defect binding energies for Xe and Kr in CeO_2 , ThO_2 , UO_2 and PuO_2 .

Subsequently, the newly parametrised potential has been used to investigate the low temperature irradiation induced athermal contribution to fission gas mobility. Thermal spike and cascade simulations have been undertaken to investigate the electronic stopping and ballistic phases of irradiation respectively.

2. Methodology

2.1. Potential model

MD simulations, employing a set of interatomic potentials for CeO₂, ThO₂, UO₂ and CeO₂ derived previously [18–20]¹, are carried out using the Large-scale Atomic/Molecular Massively Parallel Simulator (LAMMPS) [22]. In this model the potential energy of an atom with respect to all other atoms has two components - i) a pair potential description of each system and ii) a many-body embedded atom method (EAM) contribution, using the model of Daw and Baskes [24]. A more detailed description can be found in Ref. [18–20].

Although the parameters for the actinide oxide systems have been developed previously, parameters must still be derived for the interactions of Xe and Kr with the actinide and oxygen species. A detailed description of this fitting procedure follows in Section 2.2. Due to Xe and Kr being inert gases, the interactions with host cation and oxygen ions were adequately described with the purely pairwise Buckingham potential (equation 1), with no many-body, coulombic or Morse description being necessary. Note also that the gas-gas interactions used here were developed previously by Tang-Toennies [29], enabling mixed gas Xe-Kr systems to be studied.

$$\phi_B(r_{ij}) = A_{\alpha\beta} \exp\left(\frac{-r_{ij}}{\rho_{\alpha\beta}}\right) - \frac{C_{\alpha\beta}}{r_{ij}^6} \quad (1)$$

2.2. Fitting procedure

The fitting procedure for gas interactions with the host actinide oxide is conducted over three stages: i) firstly structure matching is carried out to DFT energy minimised Xe/Kr defects in CeO₂, ThO₂, UO₂ and PuO₂ to develop an initial set of potential parameters, ii) using this initial attempt, structures are generated using MD for Xe or Kr at a bound Schottky trio in CeO₂, ThO₂, UO₂ and PuO₂ at temperatures of 300 K, 1500 K, 3000 K and 5000 K (at which temperature the structure is liquid) to ensure a significant sample of representative configurations and, finally, iii) the potential parameters are readjusted to reproduce the forces on Xe and Kr predicted by DFT for these MD configurations. Stages ii) and iii) can be repeated using updated parameters until a satisfactory match is achieved. This procedure is illustrated in Figure 1 with stages i)-iii) labelled and the final parameter set is reported in Table 1. This approach aims to include insight from DFT on the temperature effects of fission gas behaviour, while avoiding computationally expensive DFT-MD calculations. In line with the fitting approach used for the actinide oxides [18], the ρ parameters are scaled to the ionic radii of the actinides involved. Gas-oxygen interactions are kept the same for all systems to enable the possibility of modelling Xe and Kr in mixed oxides. Gas-gas interactions were not fitted here and the potential developed by Tang-Toennies [29] has been used throughout. For the generation of MD configurations, calculations were carried out on $2 \times 2 \times 2$ fluorite supercells so that subsequent DFT force calculations were manageable. An NVT ensemble was used with a thermostat relaxation time of 0.1 ps at 300 K, 1500 K, 3000 K and 5000 K and a timestep of 2 fs.

2.3. DFT details

DFT calculations were carried out using with the plane-wave Vienna *ab initio* simulation package (VASP) [30] with PAW pseudo-potentials. The exchange correlation term was modelled using the generalised gradient approximation (GGA) of Perdew, Burke and Ernzeroff (PBE) [31].

¹Supplementary material describing the use of this potential for use in GULP [21], LAMMPS [22] and DL-POLY [23] are provided at <http://abulafia.mt.ic.ac.uk/potentials/actinides>

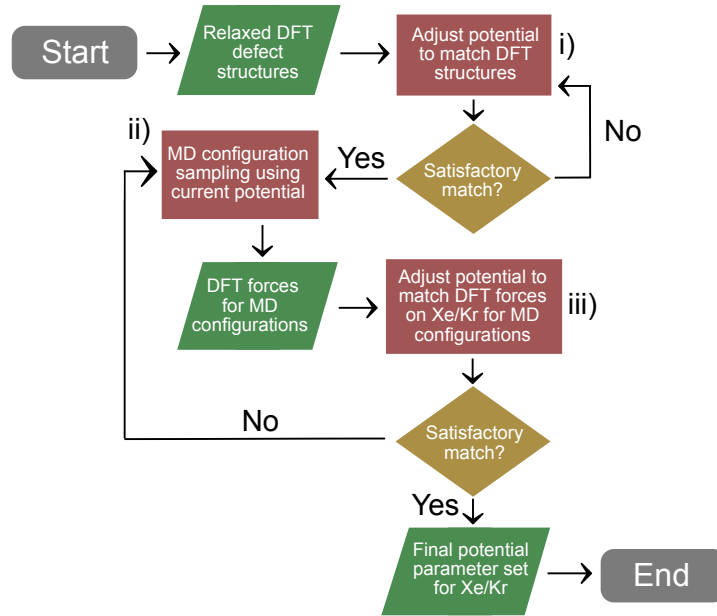


Figure 1: A schematic illustration of the fitting procedure conducted for the development of the potential parameters for Xe and Kr in CeO₂, ThO₂, UO₂ and PuO₂. The final parameter set is reported in Table 1.

A consistent plane wave cut off of 500 eV was applied to the standard projected augmented wave (PAW) potential approach. The magnetic ordering of UO₂ was described with the 1k antiferromagnetic ordering [32, 33]. CeO₂ and ThO₂ were maintained as non-magnetic. In order to describe the behaviour of the localised cation f states the orbital-dependent, Coulomb potential, U , and the exchange parameter J were used within DFT+U [34, 35]. The values of U and J for each oxide were taken from established literature data [36–39]. To include van der Waals (vdW) interactions the pairwise interactions of Grimme [40] are implemented. To avoid metastable states U-ramping was applied to the perfect supercell in advance of the defect calculations [41]. For all calculations a $2 \times 2 \times 2$ fluorite supercell was used, with $2 \times 2 \times 2$ Monkhorst-Pack k -point mesh. Gaussian smearing of bands was performed with a broadening width of 0.1 eV. Geometry relaxation of internal coordinates was achieved until the energy differences between two consecutive steps was below 1×10^{-4} eV, or all forces were less than 1×10^{-2} eVÅ⁻¹. The convergence criteria were selected on the basis that it would be difficult to fit an empirical potential to DFT forces with greater accuracy than this.

A single gas atom was used as the reference energy for the calculation of gas incorporation energies. As the only defect reactions considered maintain the charge on the supercell, it was not necessary to correct for interactions between the defect and the charge compensating background. Any such correction would cancel out (see reactions 2-4).

2.4. Radiation damage calculations

Following the development of gas potentials, MD calculations were carried out to investigate radiation damage by thermal spike and cascade simulations, representing the electronic and ballistic stopping phases of irradiation respectively. To prevent unrealistic forces at the short separations, accessed due to such high energy events, a ZBL potential was splined between 1.0 Å and 1.6 Å to the CRG+gas potential developed in this work. The next step was to create a

Table 1: Potential parameters for Xe and Kr in CeO₂, ThO₂, UO₂ and PuO₂ of the Buckingham potential form given by equation 1. Note that Coulombic, Morse and EAM potentials were not used for the gas potentials.

	Xe-O	Xe-Ce	Xe-Th	Xe-U	Xe-Pu
$A_{\alpha\beta}$ (eV)	1877.5990	6308.6510	6238.0739	6606.3980	6591.3310
$\rho_{\alpha\beta}$ (Å)	0.3401910	0.2891647	0.3130134	0.2981080	0.2861837
$C_{\alpha\beta}$ (eVÅ ⁶)	46.478139	18.013067	20.013067	19.013067	18.013067
	Kr-O	Kr-Ce	Kr-Th	Kr-U	Kr-Pu
$A_{\alpha\beta}$ (eV)	1862.8460	7885.8137	7797.5924	8257.9975	8239.1637
$\rho_{\alpha\beta}$ (Å)	0.3231814	0.2747064	0.2973627	0.2832030	0.2718745
$C_{\alpha\beta}$ (eVÅ ⁶)	39.908723	17.112414	19.012431	18.062414	17.112414

35×35×35 UO₂ supercell with 1 % uranium cations randomly replaced with Xe or Kr atoms and 1 % oxygen anions randomly removed (to maintain charge neutrality). To enable the oxygen species to migrate to the lowest energy configuration, the system was annealed at 2000 K and then cooled to the temperature of interest (600 K) in the NPT ensemble at zero pressure and using barostat and thermostat relaxation times of 0.1 ps and 0.5 ps respectively. This fully equilibrated 35 × 35 × 35 UO₂ supercell was used as the starting point for subsequent damage calculations.

Three thermal spike calculations were conducted by depositing 30 keV/nm, 50 keV/nm and 70 keV/nm of kinetic energy into a cylindrical region (axis in z direction) with a radius of 2.00 nm, 3.76 nm and 4.98 nm, respectively, at the center of a 70×70×35 UO₂ fluorite supercell (2,058,000 atoms). These radii and energies were chosen based on the post-irradiation experiments of Toulemonde *et al.* [42]. The energy was introduced by randomly rescaling the atomic velocities within the cylindrical region to the appropriate temperature with the constraint that the velocities observed a typical Boltzmann distribution. Due to the large energy deposited within the system it was necessary to use a heat bath in the region within 20 Å of the x and y periodic boundaries, whereby the atomic velocities within this boundary were rescaled every timestep to 600 K. This ensured that heat was gradually removed throughout the simulation and it returned to the initial equilibrium temperature after 170 ps. Throughout the thermal spike calculations the MSD for each species was calculated.

Cascade simulations were conducted by selecting a uranium cation and scaling its velocity in a random direction with a kinetic energy of 10 keV, 25 keV, 50 keV and 75 keV within a 70×70×70 UO₂ fluorite supercell (4,116,000 atoms). The damage cascade was subsequently allowed to evolve in the NVT ensemble until the system returned to equilibrium. The end equilibrium temperature was not sufficiently greater than 600 K to justify the use of a thermostat at the periodic boundaries. This method was repeated 15 times for each cascade energy and the mean squared displacement (MSD) for each species was determined.

3. Results and discussion

3.1. DFT defect energies

To generate defect structures for the initial stage of the fitting procedure energy minimisation calculations were carried out for Xe and Kr accommodation a number of sites in CeO₂, ThO₂, UO₂ and PuO₂. The energies for Xe or Kr (X) incorporation into an oxygen vacancy (reaction 2), cation vacancy (reaction 3) and the bound Schottky trio (reaction 4) are reported for

CeO₂, ThO₂, UO₂ and PuO₂ (see Table 2):



where reactions 5-7 use Kröger-Vink notation [43]. M and X represent the cation and gas species respective. Three Schottky trio cluster configurations were considered, whereby both oxygen vacancies occupy first nearest neighbour positions with respect to the uranium vacancy and occupy either first (SD1), second (SD2) or third (SD3) nearest neighbour positions with respect to each other. For all incorporation energies into Schottky trios, the oxygen vacancy positions are allowed to reconfigure, such that the lowest energy configuration with (RHS reaction 4) or without a gas atom (LHS reaction 4) is always used.

Table 2: DFT incorporation energies for Xe and Kr into the actinide oxides MO₂ (where M is Ce, Th, U or Pu). The resultant defect structures are used in fitting the empirical potential.

	CeO ₂ (eV)	ThO ₂ (eV)	UO ₂ (eV)	PuO ₂ (eV)
Xe _i [×]	10.56	10.19	8.94	10.70
Xe _M ^{′′′}	4.71	3.74	3.70	5.01
Xe _O ^{••}	7.68	7.50	6.85	8.80
Xe _{M:2O} [×]	0.72	0.32	0.49	0.87
Kr _i [×]	7.48	6.96	6.15	7.46
Kr _M ^{′′′}	3.31	2.64	2.49	2.66
Kr _O ^{••}	5.00	4.84	4.56	5.92
Kr _{M:2O} [×]	0.28	0.11	0.18	0.39

Table 2 shows that for Xe and Kr incorporation into all of the host systems, the lowest energies are predicted for the Schottky defect. The interstitial is the least favourable incorporation site, while incorporation at the cation site is more favourable than the oxygen site for all systems. Chemical interactions associated with the coordination environment of a given site are limited due to the noble gases being inert. Consequently, the lower incorporation energies can be understood in terms of a steric argument and are associated with defects that present a larger defect volume to accommodate the relatively large Xe and Kr atoms. Similarly, host systems with larger lattice parameters also present a greater volume for more favourable incorporation of Xe and Kr. By comparison with literature data [44–46] similar trends can be seen, whereby low incorporation energies are predicted in the bound Schottky trio. The DFT data from Thompson *et al.* [45] further supports that incorporation is more favourable at a uranium site than an oxygen site.

3.2. Fitting results

The initial set of gas parameters was iteratively refined by minimising the atomic forces predicted by the potential when using the DFT defect structures calculated in section 3.1. The empirical interatomic forces were converged to within 0.066 eVÅ⁻¹ and 0.055 eVÅ⁻¹ per atom against the DFT forces (in this case zero) for Xe and Kr defects respectively. MD configurations were sampled using the initial parameter set and then DFT atomic forces were calculated using those structures. Finally, the potential set was further refined to reproduce the DFT force acting on Xe or Kr in each of the MD generated structures. Forces on the host lattice were omitted from

fitting due to the differences between the DFT and empirical descriptions being used (e.g. slight differences in the predicted lattice parameter). Forces on Xe and Kr were refined on average to within 0.251 eV\AA^{-1} and 0.224 eV\AA^{-1} of the DFT forces respectively.

Table 1 reports the final parameter set derived for Xe-O, Xe-Ce, Xe-Th, Xe-U, Xe-Pu, Kr-O, Kr-Ce, Kr-Th, Kr-U and Kr-Pu. These parameters were derived in conjunction with the gas-gas interactions of Tang-Toennies [29] to allow mixed gas calculations. Further validation may be necessary if one wishes to use the potentials derived here with alternative gas-gas interactions.

Figure 2 shows the relaxed defect structures for Xe and Kr in the SD1 defect for the $2 \times 2 \times 2$ (DFT and empirical potential) and $10 \times 10 \times 10$ (empirical potential only) UO_2 supercells. The structure for the host SD1 defect is shown in a) with uranium and oxygen ions represented by green and red spheres respectively. The displacements of host atoms, relative to a), due to the incorporation of Xe and Kr are represented by the color gradient in b) and c). It can be seen that in all cases, regardless of supercell size, there is agreement that the most displaced atoms are the first nearest neighbour oxygen ions. For the $2 \times 2 \times 2$ supercell the empirical potential exhibits smaller displacements for ions beyond the first nearest neighbour positions. This may be due to the symmetric nature of the Buckingham potential leading to the atoms in one cell experiencing the displacement field from the surrounding cells. This was examined by calculating the displacement due to gas incorporation in the $10 \times 10 \times 10$ UO_2 supercell. Here it can be seen that greater displacement is predicted for defects beyond the first nearest neighbour ions compared to the $2 \times 2 \times 2$ supercell, giving better agreement with the DFT results. The distribution of displacements around the gas atom remains symmetrical, as expected from the centro-symmetric Buckingham potential used here combined with the symmetry of the defect.

3.3. Validation of empirical parameters

Although the agreement with force matching between DFT and the potential using static and MD based structures has been discussed, it is necessary to test the potential's predictive capabilities by comparing against properties not used during fitting. When calculating the incorporation energies in Table 2 reference energies must be used for the gas species outside of the host lattice. As there are no equivalent reference states when using the empirical potential, it is necessary to validate the potential against DFT for reactions that negate such reference states. Validation was, therefore, carried out against the binding energy of a gas interstitial with vacancy accommodation sites in CeO_2 , ThO_2 , UO_2 and PuO_2 . As neither the products nor reactants in these reactions involve any species outside the host lattice, the issue of reference energies are removed so that the DFT and empirical potential energies are directly equivalent. The potentials are validated for gas interstitial binding with an oxygen vacancy (reaction 5), a cation vacancy (reaction 6) and a bound Schottky defect (reaction 7).



In all cases the gas atom is fully incorporated with the vacancies, so that binding is in effect to the 0th nearest neighbour configuration. The binding energies associated with these reactions are given in Figure 3 for the new empirical potential (parameters reported in Table 1) and for DFT using the formation energies calculated in Section 3.1 (see Table 2). Where possible, comparison has also been made to literature DFT results [14, 44–46] [Meis and Chartier]. Figure 3 shows similar trends for the binding energies for Xe and Kr defects in CeO_2 , ThO_2 , UO_2 and PuO_2 between the empirical potential and the DFT methods used in this paper. Additionally,

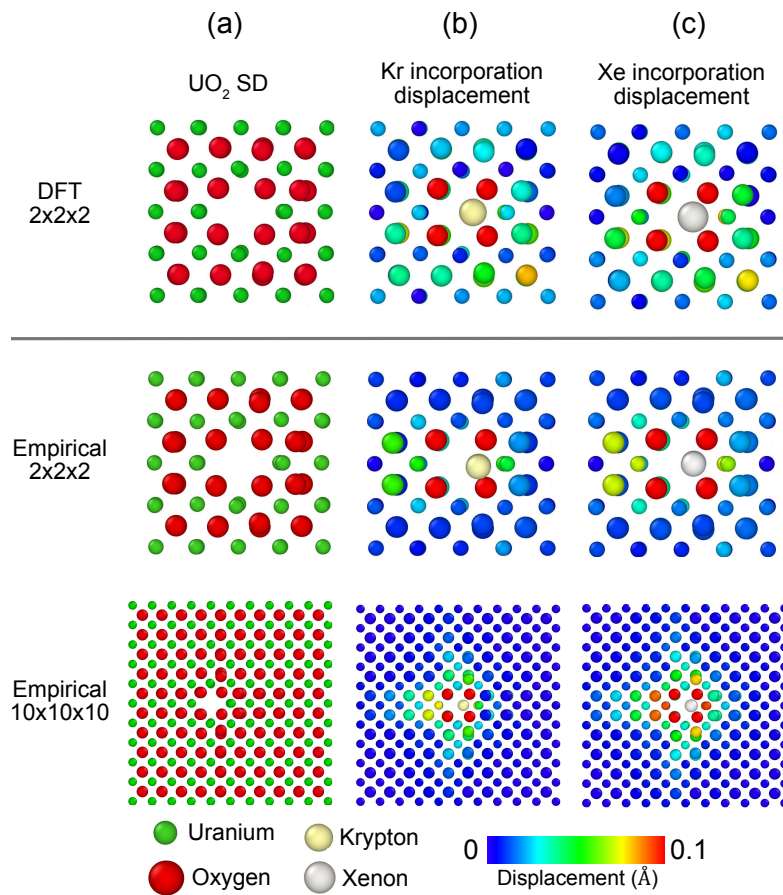


Figure 2: a) The SD1 defect structure predicted by DFT and the empirical potential in $2 \times 2 \times 2$ and $10 \times 10 \times 10$ UO_2 supercells is shown. Oxygen and uranium ions are represented by red and green spheres respectively. b) and c) shows the displacement of U and O atoms relative to a) due the incorporation of Xe and Kr. The color of the U and O atoms in b) and c) corresponds to the magnitude of the displacement. Xe and Kr atoms are shown by grey and beige spheres respectively.

for UO_2 the empirical values lie within the scatter shown by literature DFT data. The origin of variation in DFT values may lie in the different method implemented (e.g. LDA vs GGA). For all cases binding energies are lower for Kr than Xe regardless of the system studied. This is expected as Xe has a greater atomic radius than Kr and it is, therefore, expected to exhibit stronger binding energies to vacancy defects, which provide more space relative to the interstitial site. Similarly, Xe and Kr both exhibit the most negative (strongest) binding energies with the Schottky defect across all host systems, due to the large volume presented by this defect. The data for the empirical potential developed by Chartier *et al.* [48] have been included in Figure 3, revealing similar trends to the potential developed in this work. However, the new potential predicts stronger binding for all defects compared to Chartier *et al.*.

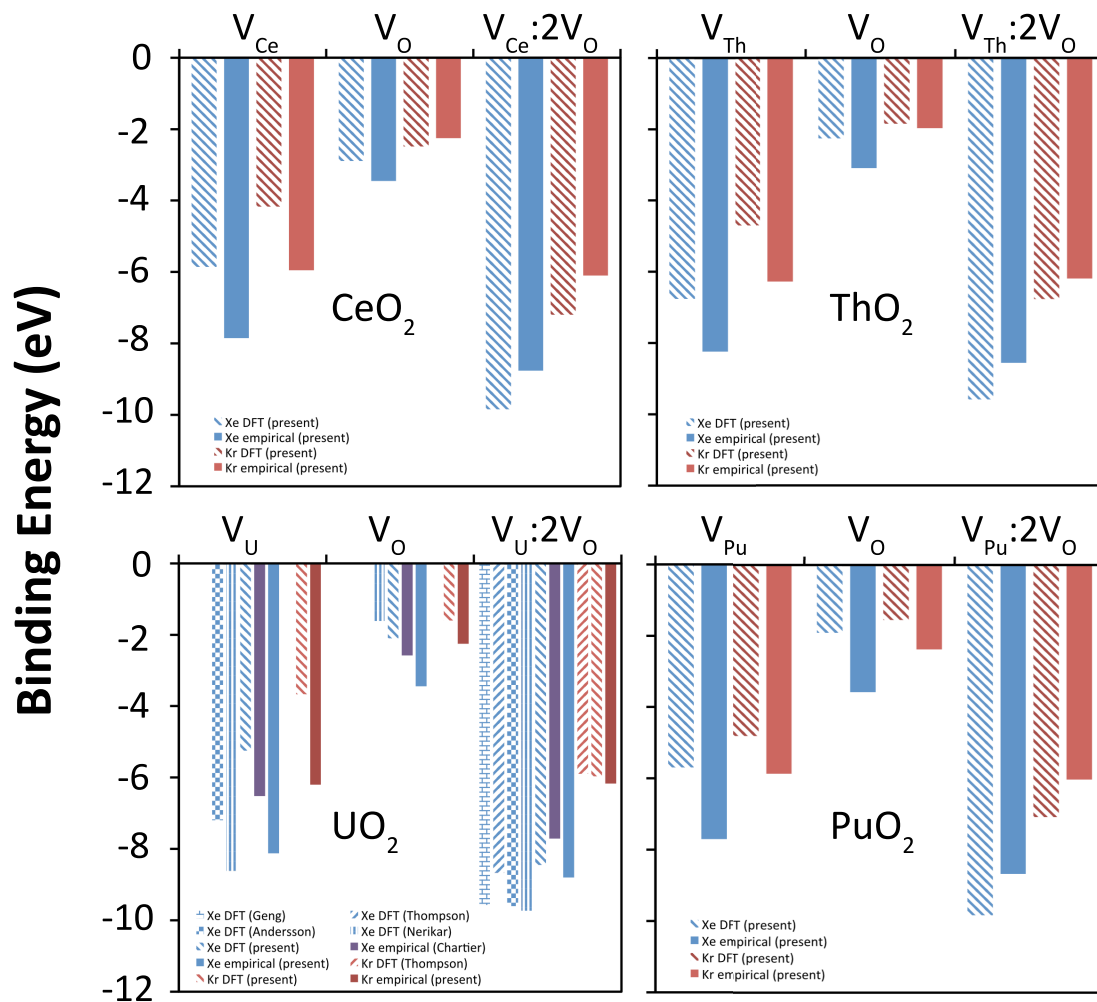


Figure 3: The binding energy for the incorporation of a Xe (blue) or Kr (red) atom starting at the interstitial site into an oxygen vacancy (reaction 5), uranium vacancy (reaction 6) or Schottky defect (reaction 7). DFT results (partially filled columns) are reported from the literature [14, 44–46] and the present study (using Table 2) for comparison with the new empirical potential potential (solid columns). The empirical data of Chartier *et al.* [48] are also reported.

3.4. Diffusion during the ballistic phase of irradiation

Having derived a new gas potential with a focus on accurately describing behaviour over a broad range of temperatures we now have the tools necessary to investigate fission gas diffusion during irradiation. As discussed in the methodology damage cascade simulations were carried out with PKA energies of 10 keV, 25 keV, 50 keV and 75 keV. For each energy 15 PKA directions were chosen randomly so that a statistical average could be obtained. Figure 4 shows the evolution of the temperature profile during a 75 keV cascade (red and blue semi-transparent regions indicate hot and cold respectively, atoms below 600 K have been removed). The opaque spheres indicate displaced Xe atoms, whereby their color identifies the magnitude of displacement relative to the initial configuration. It can be seen that the PKA rapidly recoils and causes branching within the first 0.01 ps. Further branching occurs within the next few ps as the cascade spreads out. By 20 ps it can be seen that significant Xe displacement has occurred and the cascade is beginning to cool down. Finally by 30 ps the cascade energy has more or less fully dissipated and the Xe atoms are permanently displaced from their original configuration. Note that, although not shown here for clarity, there is also displacement of the host U and O ions.

Figure 5 shows the evolution of the number of Frenkel pairs, counted using a Wigner-Seitz analysis, and the mean squared displacement of U, O and Xe during the simulation of a 75 keV damage cascade. It can be seen that initially the number Frenkel pairs increases and quickly reaches a peak. Subsequently, the lattice recovers leaving residual damage in the lattice. On the contrary the mean squared displacement of all three species increase and, although it oscillates due to shock waves, it does not recover. As the lattice recovers the species settle down at lattice sites displaced from the original configuration; atomic mixing has occurred. The simulation was continued for an additional 100 ps until the oscillations had settled down. This was repeated for several PKA energies and the mean squared displacement of U, O, Kr and Xe as a function of PKA energy is shown in Figure 6. It is clear that O and Kr mix the most during cascade simulations and U the least, while Xe lies in between. This is more clearly seen by calculating the mean squared displacement per unit PKA energy, from which the diffusivity can be calculated (see Figure 7) using the typical in-reactor cascade parameters reported previously [49]. The estimated diffusivity is around 2 orders of magnitude too low compared to the experiment data of Turnbull *et al.* [7]. Thus, the ballistic phase of radiation damage does not account for all of the atomic mixing. It is hypothesised that the majority of atomic mixing must occur during the electronic stopping phase, which has been investigated by thermal spike calculations.

3.5. Diffusion during the electronic stopping phase of irradiation

Preliminary thermal spike calculations to investigate the electronic stopping phase have been carried out for cylindrical spikes with 30 keV/nm, 50 keV/nm and 70 keV/nm. As for the cascade simulations, this results in a very high energy event at the center of the simulation cell that gives rise to significant atomic mixing. Figure 8 shows the high temperature region of a thermal spike 70 ps after its initiation, semi-transparent spheres indicate the local temperature and atoms at 600 K or below have been removed. The opaque balls represent displaced Xe, whereby the color indicates the displacement relative to the original configuration. The cylindrical shape of the thermal spike is evident and a great deal of atomic mixing has occurred in the middle of the spike where the lattice has melted.

Figure 9 shows the preliminary results from 3 thermal spikes that have ran for 127 ps for the mean squared displacement of U, O and Xe as a function of energy deposited into the lattice per unit length. It is clear that O diffusion exceeds that of Xe, which exceeds that of U, in agreement with the results on the ballistic phase (Figure 6). Repeats must be conducted at these energies, in addition to further low energy calculations to determine if there is a cut off

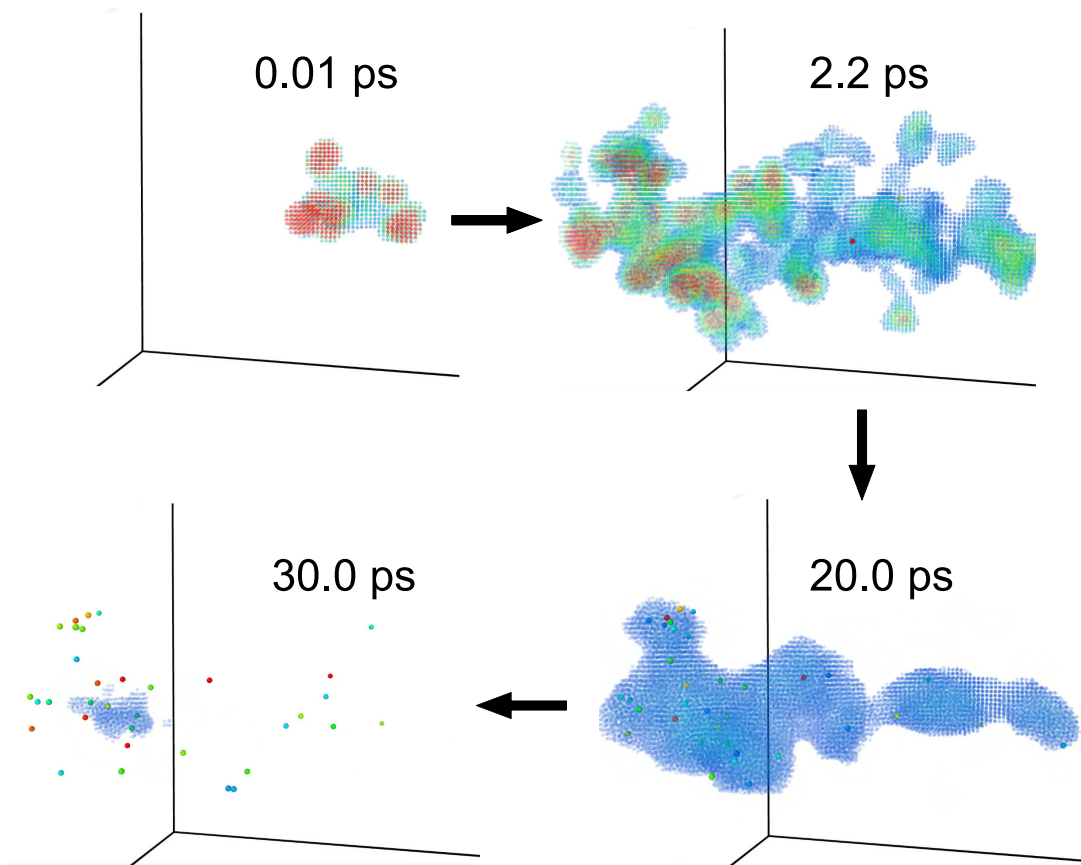


Figure 4: Visualization of a damage cascade with a PKA energy of 75 keV. The U and O atoms are represented by semi-transparent spheres, whereby their color indicates the local temperature (red and blue being hot and cold respectively). Atom with kinetic energy below 600 K are removed. Displaced Xe atoms are represented by opaque spheres, whereby their color indicates the displacement relative to the initial configuration (red indicates displacement greater than 5 Å).

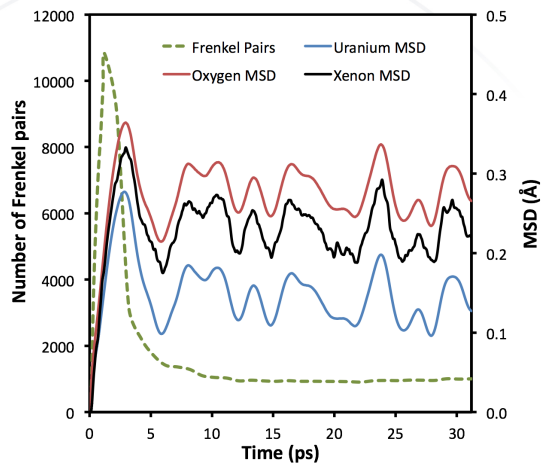


Figure 5: The time evolution of the total number of Frenkel defects in the system (green) as well as the MSD of U (blue), O (red) and Xe (black), during a 75 keV damage cascade.

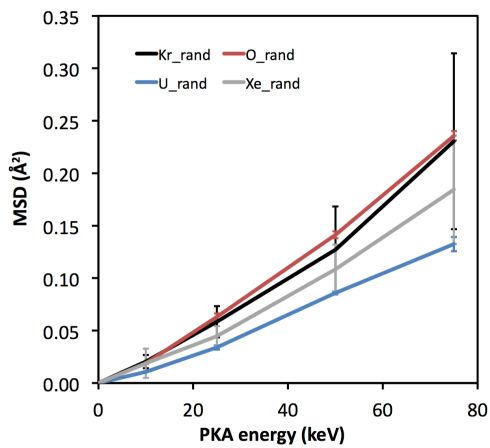


Figure 6: The MSD of U (blue), O (red), Xe (grey) and Kr (black) at the end of cascade simulations as a function of the PKA energy. Each point is the average of 15 such simulations and error bars indicate the standard deviation.

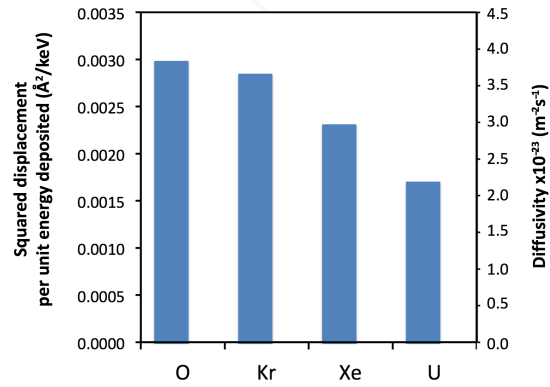


Figure 7: By fitting straight lines to the the data in Figure 6 the MSD per unit PKA energy is reported for each species. Using the typical in-reactor cascade parameters reported by Ref. [49] the corresponding diffusivity has been estimated.

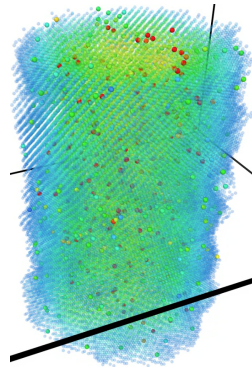


Figure 8: Visualization of a 30 keV/nm thermal spike calculation in UO₂ with 1 % Xe, 70 ps following initiation. The U and O atoms are represented by semi-transparent spheres, whereby their color indicates the local temperature (red and blue being hot and cold respectively). Atoms with kinetic energy below 600 K are removed. Xe atoms are represented by opaque spheres, whereby their color indicates the displacement relative to the initial configuration (red indicates displacement greater than 5 Å).

energy below which diffusion does not occur for the electronic phase. Subsequently, it will be possible to examine the hypothesis that electronic stopping fully accounts for the discrepancy between experiments and the cascade simulations reported in section 3.4. However, we can already assert that fission gas mobility in the athermal diffusion regime lies between that of O and U. It is important to note that the MSD in Figures 6 and 9 are not directly comparable due to the different box sizes and the units on the x -axis. Work is ongoing to derive a value for diffusivity during the electronic phase that can be compared to the ballistic phase.

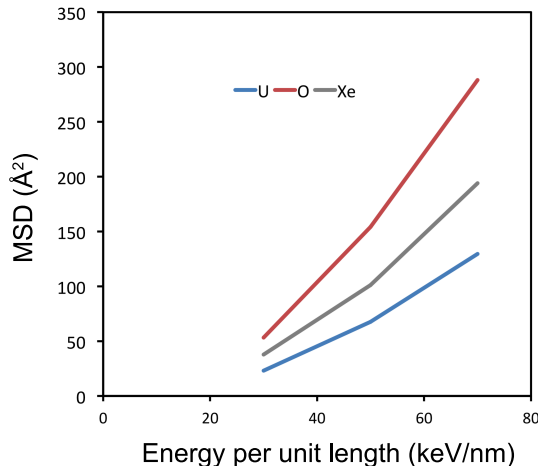


Figure 9: Preliminary results for the mean square displacement (MSD) of U (blue), O (red) and Xe (grey) at the end of thermal spike simulations as a function of the energy deposited per unit length.

Residual damage formed during the thermal spike can be seen in Figure 10 as three loop dislocations and a line dislocation. Future work should be done to investigate whether these extended defects can trap fission gas and initiate bubble formation, however this is beyond the scope of this work. Furthermore, the possibility that the diffusion behaviour may change by running a second thermal spike calculation on the damaged region of crystal should be studied.

4. Conclusions

Understanding the behaviour of fission gases in nuclear fuel is crucial for the safe and efficient operation of nuclear reactors. Atomistic simulations provide a useful tool for investigating the underlying mechanisms that govern fission gas behaviour. As such, empirical potentials that the simulations rely upon are continuously improved. In particular, when investigating diffusion due to irradiation it is important to have a potential set that can accurately describe behaviour over a broad range of temperatures. To this end we have developed a set of Xe and Kr Buckingham potentials for use with the many-body CRG potential, which was shown to more accurately describe the thermophysical properties of actinide oxides and their solid solutions over from 300 K to 3000 K. Fitting was carried out by force matching to DFT using MD generated configurations of Xe and Kr in CeO_2 , ThO_2 , UO_2 and PuO_2 at 300 K, 1500 K, 3000 K and 5000 K. This ensures the potentials provide a reasonable description of gas interactions with the host systems for Xe and Kr coordination environments relevant to the wide range of

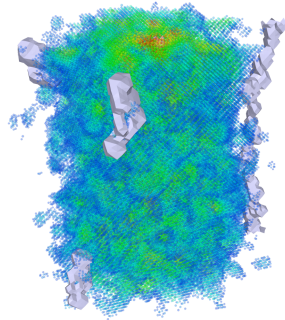


Figure 10: Visualization of a 30 keV/nm thermal spike calculation 127 ps following initiation. The color represents the local temperature (red and blue being hot and cold respectively) and atoms with kinetic energy below the background temperature of 600 K are removed. One line dislocation and three dislocation loops are visualized using grey surfaces.

temperatures experienced by nuclear fuel. The potential set is validated against literature and newly presented DFT binding energies for an interstitial gas atom being accommodated into cation, oxygen and bound Schottky vacancies. The potential parameter set creates the possibility of investigating Xe and Kr in CeO_2 , ThO_2 , UO_2 and PuO_2 including solid solutions of these end members.

Using the new potential the role of radiation damage in the low temperature diffusion of fission gas has been investigated. It was shown by cascade calculations that the ballistic phase of radiation damage is insufficient to account fully for the experimentally observed fission athermal gas contribution. Preliminary results using the thermal spike method has been implemented to study the electronic phase of irradiation. Further repeats must be carried out to quantify the contribution of the electronic stopping phase and identify if this resolves the disagreement between experiment and modelling.

Acknowledgements

This work was funded by the U.S. department of Energy, Office of Nuclear Energy, Nuclear Energy Advanced Modeling Simulation (NEAMS) program. Los Alamos National Laboratory, an affirmative action/equal opportunity employer, is operated by Los Alamos National Security, LLC, for the National Nuclear Security Administration of the U.S. Department of Energy under Contract No. DE-AC52-06NA25396. Computational resources for DFT calculations were provided by the Imperial College London HPC facility, UK, the Australian national computational infrastructure NCI-Raijin and the the multi-modal Australian sciences imaging and visualisation environment (MASSIVE). Funding for N. Kuganathan was provided by the EPSRC, grant number EP/K00817X/1, as part of the INDO-UK project.

References

- [1] Kim, Y.-E., Park, J.-W., and Cleveland, J. (2006) *IAEA-TECDOC-1496*.
- [2] Olander, D. (2009) *J. Nucl. Mater.* **389**, 1–22.

- [3] Matzke, H. (1980) *Rad. Effects* **53**, 219–242.
- [4] Une, K. and Kashibe, S. (1990) *J. Nucl. Sci. Tech.* **27**, 1002–1016.
- [5] White, R. J. and Tucker, M. O. (1983) *J. Nucl. Mater.* **118**, 1–38.
- [6] Tonks, M. R., Liu, X.-Y., Andersson, D. A., Perez, D., Chernatynskiy, A., Pastore, G., Stanek, C. R., and Williamson, R. (2016) *J. Nucl. Mater.* **469**, 89–98.
- [7] Turnbull, J. A., Friskney, C. A., Findlay, J. R., Johnson, F. A., and Walter, A. J. (1982) *J. Nucl. Mater.* **107**, 168–184.
- [8] Popov, S. G., Ivanov, V. K., Carbajo, J. J., and Yoder, G. L. (2000), "*Thermophysical properties of MOX and UO₂ fuels including the effects of irradiation*", ONRL Rep., ORNL/TM-2000/351.
- [9] Lee, W. E., Gilbert, M., Murphy, S. T., and Grimes, R. W. (2013) *J. Am. Ceram. Soc.* **96**, 2005–2030.
- [10] Sokolov, F., Kukuda, K., and Nawada, H. P. (2005), *Thorium fuel cycle - Potential benefits and challenges*, IAEA-TECDOC-1450.
- [11] Park, Y. S., Kolman, D. G., Ziraffe, H., Haertling, C., and Butt, D. P. (1999) *MRS Proceedings* **556**, 129–134.
- [12] Nelson, A. T., Rittman, D. R., White, J. T., Dunwoody, J. T., Kato, M., and McClellan, K. J. (2014) *J. Am. Ceram. Soc.* **97**, 3652–3659.
- [13] Nerikar, P. V., Parfitt, D. C., Casillas Trujillo, L. A., Andersson, D. A., Unal, C., Sinnott, S. B., Grimes, R. W., Uberuaga, B. P., and Stanek, C. R. (2011) *Phys. Rev. B* **84**, 174105.
- [14] Andersson, D. A., Uberuaga, B. P., Nerika, P. V., Unal, C., and Stanek, C. R. (2011) *Phys. Rev. B* **84**, 054105.
- [15] Turnbull, J. A. (1971) *J. Nucl. Mater.* **38**, 203–212.
- [16] Schwen, D., Huang, M., Bellon, P., and Averbach, R. S. (2009) *J. Nucl. Mater.* **392**, 35–39.
- [17] Parfitt, D. C. and Grimes, R. W. (2009) *J. Nucl. Mater.* **392**, 28–34.
- [18] Cooper, M. W. D., Rushton, M. J. D., and Grimes, R. W. (2014) *J. Phys. Condens. Matter* **26**, 105401.
- [19] Cooper, M. W. D., Murphy, S. T., Fossati, P. C. M., Rushton, M. J. D., and Grimes, R. W. (2014) *Proc. R. Soc. A Math. Phys. Eng. Sci.* **470**, 20140427.
- [20] Cooper, M. W. D., Murphy, S. T., Rushton, M. J. D., and Grimes, R. W. (2015) *J. Nucl. Mater.* **461**, 206–214.
- [21] Gale, J. D. (1997) *J. Chem. Soc. Faraday Trans.* **93**, 629–637.
- [22] Plimpton, S. (1995) *J. Comp. Phys.* **117**, 1–19.
- [23] Todorov, I. T., Smith, W., Trachenko, K., and Dove, M. T. (2006) *J. Mater. Chem.* **16**, 1911–1918.
- [24] Daw, M. S. and Baskes, M. I. (1984) *Phys. Rev. B* **29**, 6443–6453.

- [25] Ewald, P. P. (1921) *Ann. Phys.* **369**, 253–287.
- [26] Hockney, R. W. and Eastwood, J. W. (1988) *Computer simulation using particles*, Bristol, PA: Taylor & Francis.
- [27] Morse, P. (1929) *Phys. Rev.* **34**, 57–64.
- [28] Buckingham, R. A. (1938) *Proc. R. Soc. Lond. A Math. Phys. Eng. Sci.* **168**, 264–283.
- [29] Tang, K. T. and Toennies, J. P. (2003) *J. Chem. Phys.* **118**, 4976–4983.
- [30] Kresse, G. and Furthmüller, J. (1996) *Phys. Rev. B* **54**, 11169–11186.
- [31] Perdew, J. P., Burke, K., and Ernzerhof, M. (1996) *Phys. Rev. Lett.* **77**, 3865.
- [32] Dorado, B., Freyss, M., Amadon, B., Bertolus, M., Jomard, G., and Garcia, P. (2013) *J. Phys.: Condens. Matter* **25**, 333201.
- [33] Dorado, B. and Garcia, P. (2013) *Condens. Matter Phys.* **87**, 18–20.
- [34] Lichtenstein, A. I., Anisimov, V. I., and Zaanen, J. (1995) *Phys. Rev. B* **52**, R5467.
- [35] Dudarev, S. L., Botton, G. A., Savrasov, S. Y., Humphreys, C. J., and Sutton, A. P. (1998) *Phys. Rev. B* **57**, 1505.
- [36] Keating, P. R. L., Scanlon, D. O., Morgon, B. J., Galea, N. M., and Watson, G. W. (2012) *J. Phys. Chem. C* **116**, 2443–2452.
- [37] Sevik, C. and Çağun, T. (2009) *Phys. Rev. B* **80**, 014108.
- [38] Dorado, B., Jomard, G., Freyss, M., and Bertolus, M. (2010) *Phys. Rev. B* **82**, 035114.
- [39] Wang, H. and Konashi, K. (2012) *J. Alloys and Comp.* **533**, 53–57.
- [40] Grimme, S. (2006) *J. Comput. Chem.* **27**, 1787–1799.
- [41] Meredig, B., Thompson, A., Hansen, H. A., and Wolverton, C. (2010) *Phys. Rev. B* **82**, 2–6.
- [42] Toulemonde, M., Benyagoub, A., Trautmann, C., Khalfouli, N., Boccanfuso, M., Dufour, C., Gourbilleau, F., Grob, J. J., Stoquert, J. P., Costantini, J. M., Haas, F., Jacquet, E., Voss, K.-O., and Meftah, A., (2012) *Phys. Rev. B* **85**, 054112.
- [43] Kröger, F. A. and Vink, H. J. (1956) *Solid State Ionics* **3**, 307–435.
- [44] Geng, H. Y., Chen, Y., Kaneta, Y., Motoyasu, K., and Wu, Q. (2010) *Phys. Rev. B* **82**, 094106.
- [45] Thompson, A. E. and Wolverton, C. (2011) *Phys. Rev. B* **84**, 134111.
- [46] Nerikar, P., Liu, X.-Y., Uberuaga, B. P., Stanek, C. R., and Sinnott, S. B. (2009) *J. Phys.: Condens. Matter* **21**, 1–11.
- [47] Shannon, R. D. (1976) *Acta. Cryst. A*, 751.
- [48] Chartier, A., Van Brutzel, L., and Freyss, M. (2010) *Phys. Rev. B* **81**, 17411.
- [49] Martin, G., Maillard, S., Van Brutzel, L., Garcia, P., Dorado, B., and Valot, C. (2010) *J. Nucl. Mater.* **385**, 351–357.